Steel and Composite Structures, *Vol. 32, No. 2 (2019) 199-212*
DOI: https://doi.org/10.12989/scs.2019.32.2.199

Seismic behavior of Q690 circular HCFTST columns under constant axial loading and reversed cyclic lateral loading

Jiantao Wang [a] and Qing Sun [*]

Department of Civil Engineering, Xi'an Jiaotong University, Xianning West Road No. 28, Xi'an, P.R. China

(*Received December 24, 2018, Revised March 21, 2019, Accepted June 1, 2019*)

Abstract. This paper presents an investigation on seismic behavior of out-of-code Q690 circular high-strength concrete-filled thin-walled steel tubular (HCFTST) columns made up of high-strength (HS) steel tubes (yield strength $f_y \geq 690$ MPa). Eight Q690 circular HCFTST columns with various diameter-to-thickness (D/t) ratios, concrete cylinder compressive strengths (f_c) and axial compression ratios (n) were tested under the constant axial loading and reversed cyclic lateral loading. The obtained lateral load-displacement hysteretic curves, energy dissipation, skeleton curves and ductility, and stiffness degradation were analyzed in detail to reflect the influences of tested parameters. Subsequently, a simplified shear strength model was derived and validated by the test results. Finally, a finite element analysis (FEA) model incorporating a stress triaxiality dependent fracture criterion was established to simulate the seismic behavior. The systematic investigation indicates the following: compared to the D/t ratio and axial compression ratio, improving the concrete compressive strength (e.g., the HS thin-walled steel tube filled with HS concrete) had a slight influence on the ductility but an obvious enhancement of energy dissipation and peak load; the simplified shear strength model based on truss mechanism accurately predicted the shear-resisting capacity; and the established FEA model incorporating steel fracture criterion simulated well the seismic behavior (e.g., hysteretic curve, local buckling and fracture), which can be applied to the seismic analysis and design of Q690 circular HCFTST columns.

Keywords: Q690 circular HCFTST columns; seismic behavior; deteriorating behavior; simplified shear strength model; stress triaxiality dependent fracture criterion

1. Introduction

The concrete-filled steel tubular (CFST) columns have been widely applied in the construction of modern buildings and bridges, owing to their remarkable structural benefits of high strength and fire resistance, favorable ductility and large energy absorption capacity (Han *et al*. 2014, Xue *et al*. 2018). In recent years, with improvements in production techniques, high-strength (HS) steel (yield strength $f_y \geq 690$ MPa) and HS concrete (cylinder compressive strength $f_c \geq 60$ MPa) have grown commercially competitive in engineering construction because of their lighter weight and the reduced amounts of materials and labors employed (Li *et al*. 2016, Zhu *et al*. 2017, Javidan *et al*. 2018). Utilizing HS materials in CFST structures gradually captures much attention to satisfy the higher demands of performance-based design as the engineering structures develop towards the tendency of ultrahigh-rise building, long span and heavy load bearing capacity (Portoles *et al*. 2013). During the past decades, many quasi-static cyclic loading tests have been carried out to investigate the seismic behavior of traditional CFST columns, mainly focusing on the normal-strength (NS) concrete and steel (Sakino 1981, Usami and Ge 1994, Boyd *et al*. 1995, Hajjar *et al*. 1997, Nakanishi *et al*. 1999, Marson and Bruneau 2004, Fam *et al*. 2004, Han and Yang 2005, Han *et al*. 2006, Huang *et al*. 2018); therefore, considerable efforts have been conducted to help understand the seismic performance for better structural design and application.

Until now, few experimental studies have been carried out on circular CFST columns made with HS steel and HS concrete. Elremaily and Azizinamini (2002) examined the seismic behavior of circular CFST columns made of 372 MPa steel tubes filled with concrete ranging from 40 MPa to 104 MPa; Varma *et al*. (2002, 2004) investigated the behavior of square CFST columns made of steel tubes ranging from 269 MPa to 660 MPa and infill concrete of 110 MPa; Inai *et al*. (2004) examined the seismic performance of circular and square CFST columns with steel tubes from 323 MPa to 837 MPa and concrete from 35.5 MPa to 94.5 MPa; Skalomenos *et al*. (2016) examined the behavior of circular and square CFST columns with steel tubes from 387 MPa to 788 MPa and concrete from 42.4 MPa to 82.3 MPa. From the above studies, Elremaily and Azizinamini (2002), and Varma *et al*. (2002, 2004) did not observe the influences of yield strength of steel and concrete compressive strength on curvature ductility of CFST columns; Inai *et al*. (2004) concluded that the ductility of CFST columns increases as the steel strength increases, and generally decreases as the concrete strength increases; Skalomenos *et al*. (2016) concluded that the CFST columns made with HS steel experience large inelastic deformations without significant damage, even

*Corresponding author, Ph.D., Professor,
E-mail: sunq@mail.xjtu.edu.cn
[a] Ph.D. Candidate, E-mail: wangjiantao@stu.xjtu.edu.cn

ISSN: 1229-9367 (Print), 1598-6233 (Online)

though a lower ductility capacity is provided by HS steel.

Consequently, different conclusions regarding the influence of HS steel were derived from the aforementioned literatures (Elremaily and Azizinamini 2002, Varma *et al*. 2002, 2004, Inai *et al*. 2004, Skalomenos *et al*. 2016). In traditional views, the strength of the steel and the concrete should be suitably matched to improve the structural performance, and it is appropriate to utilize the combinations of higher strength steel with higher strength concrete, and lower strength steel with lower strength concrete (Han *et al*. 2014). However, using HS steel tubes in CFST columns may have large diameter-to-thickness (D/t) ratios that exceed the limitations of current design standards, e.g., American AISC 360-16 [$D/t \leq (0.15E_s/f_y)$] and Chinese GB 50936-2014 [$D/t \leq (31725/f_y)$]. Regarding the circular CFST columns using HS steel, an uncertainty in composite action still exists due to the out-of-code D/t ratios. Additionally, the experimental studies on the seismic behavior of CFST columns using HS steel are still insufficient under the out-of-code D/t ratios, and the corresponding design methods are not included in most specifications yet. When suffered earthquake motions, the severe failure in plastic hinge regions of CFST columns can result in the progressive collapse of structures after the several inelastic cycles, especially for the local buckling and fracture of HS steel structures (Zhang *et al*. 2009). Therefore, more researches are urgently needed in CFST structures, mainly focusing on the influences of HS and thin-walled steel tubes on seismic behavior of CFST columns; and an efficient method is also required to predict the non-negligible local buckling and fracture of HS steel.

Therefore, this study aimed to examine the seismic behavior of out-of-code Q690 circular high-strength concrete-filled thin-walled steel tubular (HCFTST) columns made up of high-strength steel tubes (yield strength $f_y \geq 690$ MPa). Eight Q690 circular HCFTST columns with various D/t ratios, concrete cylinder compressive strengths (f_c) and axial compression ratios (n) were tested under the combined action of constant axial loading and reversed cyclic lateral loading. Subsequently, a simplified shear strength model was derived and validated by the test results. Finally, a finite element analysis (FEA) model incorporating a stress triaxiality dependent fracture criterion was developed to simulate the seismic behavior (e.g., hysteretic curve, local buckling and fracture). Accordingly, this study can provide valuable references for the design and application of Q690 circular HCFTST columns.

2. Experimental program

2.1 Specimens

A total of eight Q690 circular HCFTST columns, divided into two groups, were designed with various combinations of D/t ratios, concrete cylinder compressive strengths (f_c) and axial compression ratios (n) through the orthogonal experimental design (Gupta *et al*. 1982, Hedayat *et al*. 2012). The tested parameters and varied levels satisfied the orthogonal arrays of $L_4(2^3)$, where L denotes the label tag; 4 is the specimen number of every test group; the superscript 3 denotes the number of tested parameters; and 2 indicates the varied levels of every parameter. A summary of the specimens is presented in Table 1. To identify the types of specimens, the notation HCFTST – $\otimes - \oplus - *$ was adopted, where $\otimes$ indicates the D/t ratio; $\oplus$ represents the concrete strength (f_c); and * represents the axial compression ratio (n).

The designed details of the tested specimens are shown in Fig. 1. The clear height of the HCFTST column was 525 mm, and a reinforced concrete (RC) foundation was cast together with the column for the convenience of applying lateral load. The cross-section sizes of the RC foundations were 1200×450×420 mm (length×width×height) and 1200×500×420 mm, and the former was adopted by the HCFTST columns with a diameter of 180 mm, while the latter was applied to other specimens. Moreover, the end-plate II was welded at the top of the tested column for loading, and the HS steel bars and stiffening ribs were utilized to strengthen the RC foundations. To ensure the construction qualities of HS steel tubes and HS concrete, the automatic metal active-gas welding and the autoclaved curing technology were employed, respectively.

2.2 Material properties

Regarding the Q690 steel, the coupon test was

Table 1 Summary of the tested specimens

Number	Group	Specimen	D/mm	t/mm	Steel grade	D/t ratio	Concrete grade	n
1	I	HCFTST-1-1-2	180	2	Q690	90	NS-1	0.2
2		HCFTST-1-4-3	180	2	Q690	90	HS-2	0.3
3		HCFTST-2-1-3	220	2	Q690	110	NS-1	0.3
4		HCFTST-2-4-2	220	2	Q690	110	HS-2	0.2
5	II	HCFTST-1-2-1	180	2	Q690	90	NS-2	0.1
6		HCFTST-1-3-4	180	2	Q690	90	HS-1	0.4
7		HCFTST-2-2-4	220	2	Q690	110	NS-2	0.4
8		HCFTST-2-3-1	220	2	Q690	110	HS-1	0.1

*$n = P/(A_s f_y + 0.85 A_c f_c)$, where A_s and A_c are the cross-sectional areas of the steel tubes and core concrete, respectively; f_y and f_c are the actual strengths of steel and concrete by material property test, respectively; and P is the applied axial force. NS and HS denote the normal-strength and high-strength, respectively.

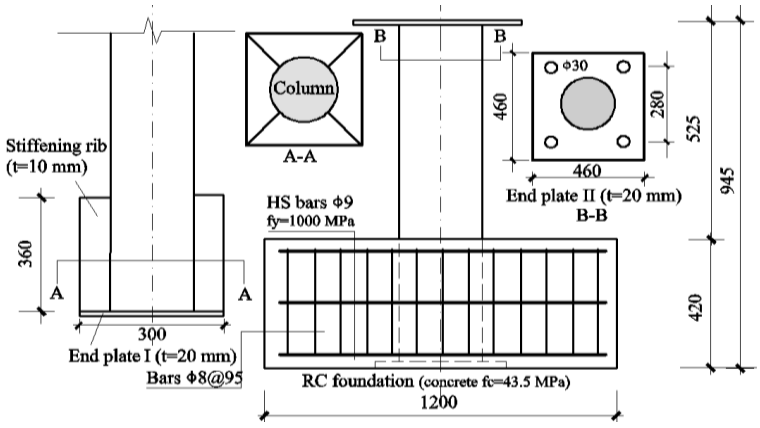

Fig. 1 Details of tested specimens (Units: mm)

Table 2 Details of concrete

Concrete grade	f_c/ MPa	Cement/ kg/m^3	Fine aggregate/ kg/m^3	Coarse aggregate/ kg/m^3	Water/ kg/m^3	Silica fume/ kg/m^3	Water reducer/ kg/m^3
NS-1	43.5	360 (Portland 425)	733	1084	170	/	13.2
NS-2	49.1	420 (Portland 425)	700	1250	135	/	12
HS-1	78.6	301 (Portland 425)	640	1310	129	129	13
HS-2	97.6	315 (Portland 525)	585	1365	120	135	13

* Portland 425 and Portland 525 denote different cement grades.

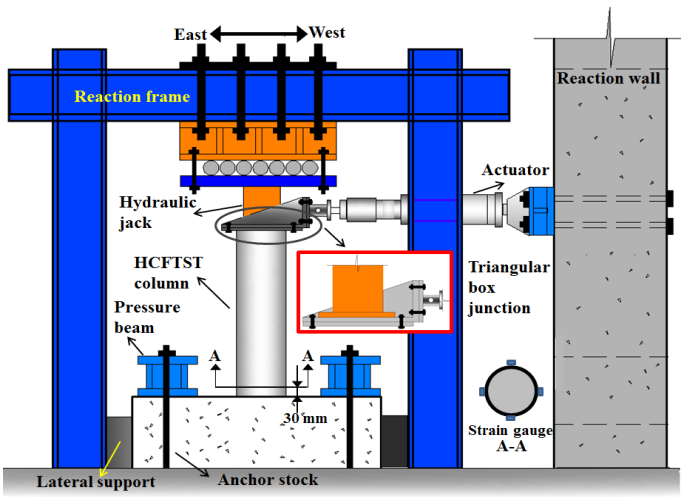

Fig. 2 Test setup

conducted to obtain the properties, in which the yield strength (f_y) and the ultimate strength (f_u) were 723 MPa and 765 MPa, respectively; and the elastic modulus (E_s) and Poisson's ratio were 222010 MPa and 0.28. The mix proportions and actual strengths (f_c) of the core concrete of HCFTST columns are listed in Table 2. The average measured compressive cylinder strengths at 28 days were 43.5 MPa (NS-1), 49.1 MPa (NS-2), 78.6 MPa (HS-1) and 97.6 MPa (HS-2).

2.3 Loading setup and program

The general features of the test setup are illustrated in Fig. 2. The RC foundation of each specimen was fully fixed using two vertical giant-sized anchor bolts, while two lateral supports were also utilized to prevent the lateral sliding of the specimen. The axial load was imposed on the column through a hydraulic jack of 2000 kN capacity; moreover, an actuator with a 1000 kN loading capacity was

(a) Local buckling

(b) Fractured steel

(c) Crushed concrete

Fig. 3 Failure modes

used to apply the cyclic lateral load. The tested column, hydraulic jack and the actuator were connected through a triangular box junction using HS bolts. A quasi-static testing method was utilized in this study. After the application of axial load, the cyclic loading procedure adopted displacement-control mode. Four single cycles were initially exerted with peak drift ratios of Δ/L = 0.10%, 0.25%, 0.50% and 0.75%, where Δ denotes the lateral displacement and L denotes the length of the column; subsequently, three cycles were performed at each peak drift ratio from 1% to 8%. Once no evident failure appeared after reaching a drift ratio of 8%, the test was continued by applying a drift ratio of 10% until the specimen failed.

The transducer inside the actuator automatically recorded the horizontal load and displacement, and the pressure cell mounted in the hydraulic jack monitored the maintained axial load. Horizontal movement at the point of loading caused by specimen rotation during each cycle resulted in the angle between the transducer and the horizontal varying by less than ±2°. No adjustments to the drift recorded by the actuator were made due to the negligible error. Four strain gauges, in an equal interval layout, were mounted on the column base to measure the longitudinal and circumferential strain. The test ended when the specimen could not sustain the targeted axial force owing to the severe failure, or when the lateral load degraded beyond 30% of the maximum experienced load.

3. Experimental results and discussion

3.1 Failure modes

Through the statistics of test phenomena, the tiny local buckling occurred at the drift ratio 2%~3% in the compressive side of the column base, except for the specimen HCFTST-1-2-1 at the first cycle of drift 4%. With continuing loading, the local buckling gradually grew until the steel tube, at 7%~8% drift, fractured with a sudden drop in lateral load. A summary of the failure modes are displayed in Fig. 3, including the severe local buckling, fractured steel tube and crushed concrete.

In Fig. 3(a), an elephant foot shaped buckling occurred in loading plane. In Fig. 3(b), the rupture crack almost penetrated the cross section, and the concrete detritus could be observed clearly through the crack. Subsequently, the specimen HCFTST-2-4-2 with the severest cross-sectional failure was incised to examine the failure mode of HS core concrete. Apparently, the HS core concrete experienced serious shear failure with a smooth fracture surface (Fig. 3(c)). It was because that the thin-walled steel tube could not restrain the expansion of shear cracks under an ultra-large D/t ratio (110) combined with a lower axial compression ratio (n = 0.2).

3.2 Load-displacement hysteretic curves

Fig. 4 shows the hysteretic curves of all tested HCFTST columns, in which the points of local buckling and fracture were marked. The tested specimens exhibited an initial elastic response, after which the columns entered an elastic-plastic process accompanied by a gradual degradation in the stiffness. In general, the local buckling occurred at 2%~3% drift ratio, and the fracture of the steel tube appeared until reaching 7%~8% drift. Apparent softening platforms of the post-peak stages existed in the hysteretic loops when the lateral loads transitioned from unloading to reloading. Moreover, the specimens (e.g., HCFTST-1-1-2 and HCFTST-1-2-1) with the NS concrete (f_c = 43.5 MPa, 49.1 MPa) and lower axial compression ratios ($n \leq 0.2$) performed slim hysteretic loops, reflecting that the HS thin-walled steel tube matched with the NS core concrete could hardly motivate enough composite action for enhancing seismic behavior under the lower axial compression ratio. Contrarily, the relatively plump hysteretic curves were achieved by a combination (e.g., HCFTST-2-1-3 and HCFTST-2-2-4) of HS thin-walled steel tube filled with the NS concrete under a larger axial compression ratio ($n \geq 0.3$). Additionally, the combination (e.g., HCFTST-1-4-3 and HCFTST-1-3-4, HCFTST-2-4-2 and HCFTST-2-3-1) of HS thin-walled steel tube matched with the HS core concrete (f_c = 78.6 MPa, 97.6 MPa) tended to perform the plump hysteretic curves regardless of larger or lower axial compression ratios. Consequently, in comparison with the aforementioned traditional points (Han *et al*. 2014), the optimized collocation, regarding the HCFTST columns, of HS thin-walled steel tube and core concrete can barely be achieved by a straightforward strength match if neglecting the effect of axial compression ratio.

3.3 Energy dissipation

The structural hysteretic loops can reflect the energy dissipation capacity. The more structure dissipates energy,

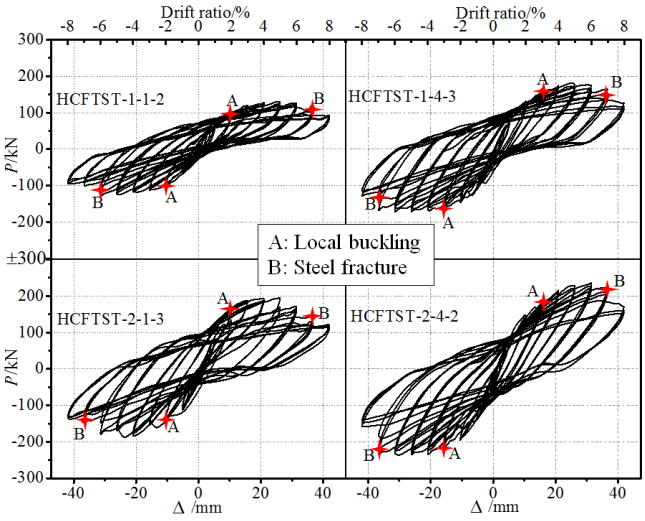

(a) Hysteretic curves of group I

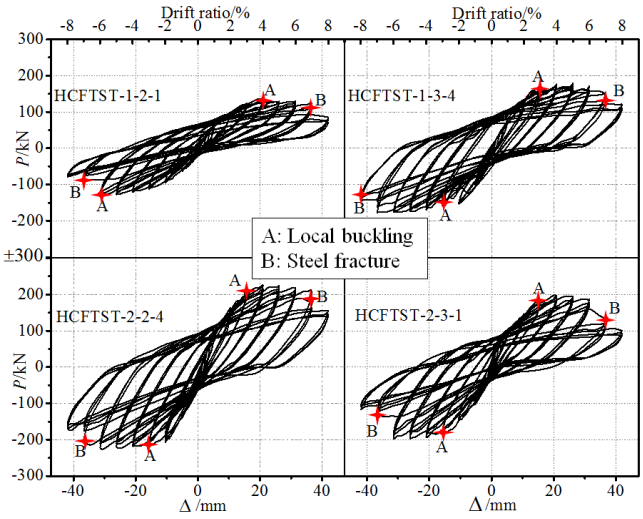

(b) Hysteretic curves of group II

Fig. 4 Hysteretic curves

the more safe structure and the less likely to be damaged. In this study, the dissipated energy of every hysteretic loop was calculated by the area integral, as shown in Figs. 5 and 6. The loop energy of different drift levels amplified gradually with the increase in lateral deflection; however, the loop energy decreased gradually within the same drift deformation, owing to the cumulative damage caused by cyclic loading. The specimens (e.g., HCFTST-1-1-2 and HCFTST-1-2-1) with the NS concrete and lower axial compression ratios demonstrated a weaker energy dissipation capacity than those HCFTST columns (e.g., HCFTST-1-4-3 and HCFTST-1-3-4) with the HS core concrete and higher axial compression ratios. Furthermore, the specimen HCFTST-2-3-1 dissipated less energy than the specimen HCFTST-1-3-4, indicating that for the HCFTST columns with out-of-code D/t ratios (110), a lower axial compression ratio easily resulted in an infirm confining effect to hardly dissipate the hysteretic energy. Generally, the loop energy suddenly dropped when entering into failure stage in combination with the severe rupture of steel tube.

The accumulated energy ratio (R_{En}) could be determined by $R_{En} = \sum_{i=1}^{n} E_n / E_T$, where E_n is the accumulated energy dissipation until the nth cyclic loop, and E_T is the total ultimate dissipated energy. Fig. 7 illustrates the analysis result of accumulated energy ratio, indicating that the cumulative damage developed nonlinearly with a slow start

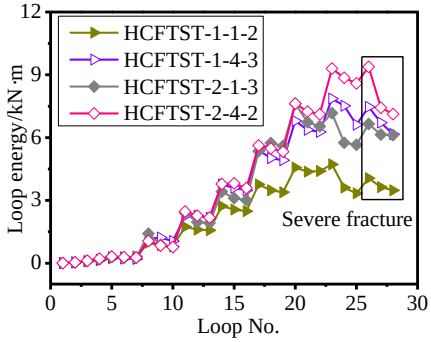

Fig. 5 Energy dissipation of group I

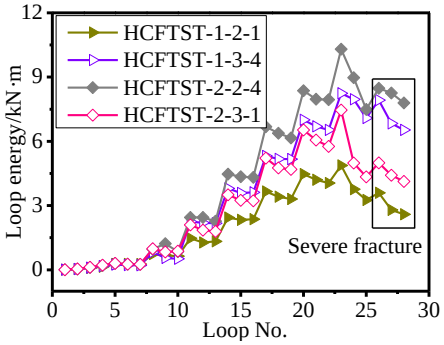

Fig. 6 Energy dissipation of group II

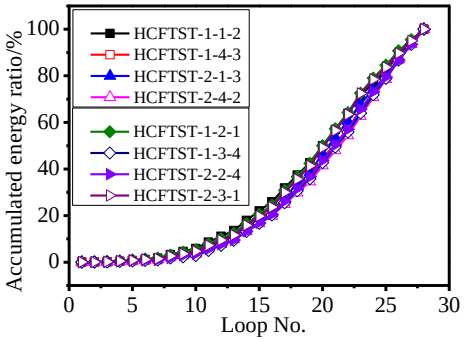

Fig. 7 Accumulated energy ratio analysis

and subsequently converted to a rapid growth after the HS thin-walled steel tube buckled. For the convenience of unified comparison, Fig. 8 demonstrates the normalized dissipated energy determined by (Zhu *et al*. 2016)

$$E_N = \sum_{i=1}^{n} [E_i / (F_i \Delta_i)] \tag{1}$$

$$\Delta_i = (\Delta_i^+ - \Delta_i^-)/2, F_i = (F_i^+ - F_i^-)/2 \tag{2}$$

where E_i and E_N are the energy dissipation of the ith loop and normalized dissipated energy, respectively; Δ_i^+ and Δ_i^- are the maximum displacements of the ith loop, respectively, in the positive and negative direction; and F_i^+ and F_i^- are the lateral loads corresponding to Δ_i^+ and Δ_i^-, respectively. Under the combination of NS concrete and lower axial compression ratios, the HCFTST columns in two groups (e.g., HCFTST-1-1-2 and HCFTST-1-2-1) had a decrease of 2.98% and 5.18% in the normalized energy dissipation, respectively, than those columns with the HS concrete and larger axial compression ratios (e.g., HCFTST-1-4-3 and HCFTST-1-3-4). However, the columns with NS concrete and larger axial compression ratios (e.g., HCFTST-2-1-3 and HCFTST-2-2-4) increased by 13.56% and 7.70%, respectively, than those columns with the HS concrete and lower axial compression ratios (e.g., HCFTST-2-4-2 and HCFTST-2-3-1), highlighting that a favorable energy dissipation capacity can be obtained by moderately increasing the axial compression ratio rather than only increasing concrete strength.

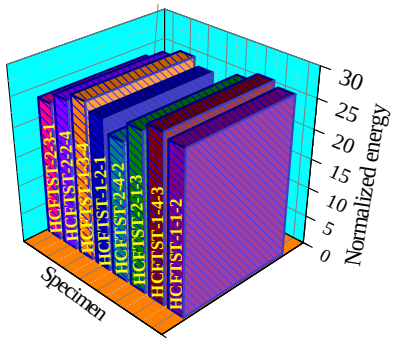

Fig. 8 Normalized dissipated energy

3.4 Skeleton curves and ductility

The skeleton curves were constructed by connecting the maximum load points at each displacement levels in accordance with the load-displacement hysteretic curves. Skeleton curves in Fig. 9 indicate that the force responses versus lateral deflections can be divided into the elastic, elasto-plastic and failure stages. To evaluate the seismic resistance, the general yield moment method (Zhou *et al*. 2012) was adopted to obtain the yield force (P_y); and subsequently, the ultimate load (P_u) was determined according to $P_u = 0.85P_m$, where P_m is the peak load. All characteristic values obtained by averaging the values of the push and pull directions are shown in Table 3, in which Δ_y, Δ_m and Δ_u are the displacements of yield load, peak load and ultimate load, respectively; u is the ductility coefficient calculated by $u = \Delta_u/\Delta_y$. It can be seen from the Table 3 that the ductility coefficients of all tested Q690 circular HCFTST columns were within the range of 2.88~3.61 and the average ductility coefficient was 3.244. A relatively reasonable ductility deformation capacity could be guaranteed though the ductility coefficient was smaller than that of traditional CFST columns (Nakanishi *et al*. 1999, Marson and Bruneau 2004, Fam *et al*. 2004). The columns (e.g., HCFTST-1-1-2 and HCFTST-2-4-2) with a lower axial compression ratio (n = 0.2) in group I had an increase of 8.52% and 15.63% in the ductility coefficient, respectively, than those columns (e.g., HCFTST-1-4-3 and HCFTST-2-1-3) with a larger axial compression ratio (n = 0.3), whereas the ductility coefficients of those columns (e.g., HCFTST-1-2-1 and HCFTST-2-3-1) with a lower

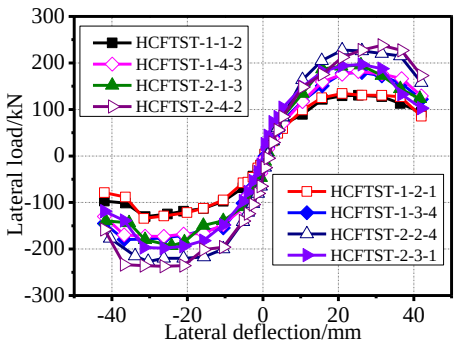

Fig. 9 Skeleton curves

Table 3 Summary of the characteristic values

Group	Specimen	P_y/kN	Δ_y/mm	P_m/kN	Δ_m/mm	P_u/kN	Δ_u/mm	u
I	HCFTST-1-1-2	93.06	10.45	130.49	28.25	110.92	35.96	3.44
	HCFTST-1-4-3	146.49	12.34	177.25	25.78	150.66	39.10	3.17
	HCFTST-2-1-3	150.41	11.42	194.19	25.10	165.06	32.89	2.88
	HCFTST-2-4-2	158.92	11.73	237.53	28.88	201.90	39.07	3.33
II	HCFTST-1-2-1	97.43	10.92	134.45	26.25	114.28	35.89	3.29
	HCFTST-1-3-4	135.34	10.77	179.48	31.48	152.56	38.89	3.61
	HCFTST-2-2-4	172.35	11.64	227.37	25.70	193.26	38.10	3.27
	HCFTST-2-3-1	154.12	11.39	197.55	26.25	167.92	33.76	2.96

axial compression ratio (n = 0.1) in group II decreased by 8.86% and 9.48%, respectively, than the columns (e.g., HCFTST-1-3-4 and HCFTST-2-2-4) with a larger axial compression ratio (n = 0.4). This phenomenon was comprehensively due to the confining effects induced by axial compression ratios in combination with the strength matching between the HS thin-walled steel tube and core concrete. Overall, the Q690 circular HCFTST columns exhibited a favorable bearing capacity to resist the lateral loading deformation.

3.5 Stiffness degradation

The secant stiffness was utilized to depict the stiffness degradation

$$K_{\text{sec}}^{i} = (K_{\text{sec}}^{i+} + K_{\text{sec}}^{i-})/2 \tag{3}$$

$$K_{\text{sec}}^{i+} = F_i^+ / \Delta_i^+, K_{\text{sec}}^{i-} = F_i^- / \Delta_i^- \tag{4}$$

where F_i^+ and F_i^- are the peak loads for the ith cycle, respectively, in the two reversal directions; Δ_i^+ and Δ_i^- are the displacements corresponding to the peak loads for the ith cycle in two directions; and K_{sec}^i is the mean secant stiffness of the ith cycle.

Fig. 10 illustrates the patterns of secant stiffness degradation for all tested columns. Despite the differences in axial compression ratios, the tested column with a HS core concrete (e.g., HCFTST-1-4-3 versus HCFTST-1-1-2, and HCFTST-2-3-1 versus HCFTST-2-2-4) tended to obtain larger initial secant stiffness owing to the higher elastic modulus of HS core concrete. Generally, the Q690 circular HCFTST columns demonstrated a snap degradation before the local buckling, and subsequently transitioned to a stable decrease until failure.

3.6 Influences of parameters

An orthogonal analysis was conducted to investigate the effects of the tested parameters (Fig. 11) on seismic behavior (Cheng 1995, Wu and Hamada 2011).

It can be observed that increasing the D/t ratio from 90 to 110 could enhance the ultimate dissipated energy (E_T) and peak load (P_m), respectively, by an average increment of 27.05% and 37.82% owing to the direct increase of cross-section size; and the ductility coefficient (u) decreased by 6.04% and 9.57%, respectively, for the group I and II. In group I, the enhancement in concrete strength from 43.5 MPa to 97.6 MPa could lead to an increment of 32.78%, 27.75% and 2.83%, respectively, for the E_T, P_m and u; in group II, the corresponding results of increasing concrete strength from 49.1 MPa to 78.6 MPa increased by 3.54%, 4.20% and 0.22%, respectively. Therefore, the HS thin-walled steel tube filled with HS concrete had a slight influence on ductility compared to the obvious enhancements of energy dissipation and peak load. Regarding the increase in axial compression ratio, the ultimate dissipated energy and peak load of the group I had an enhancement of 11.38% and 0.93%, respectively;

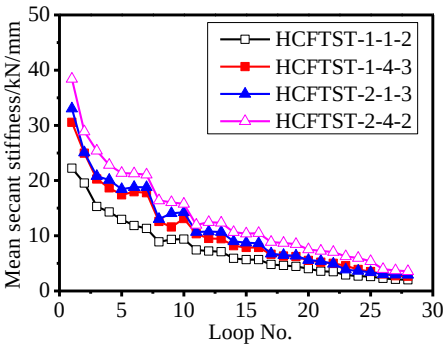

(a) Stiffness degradation of group I

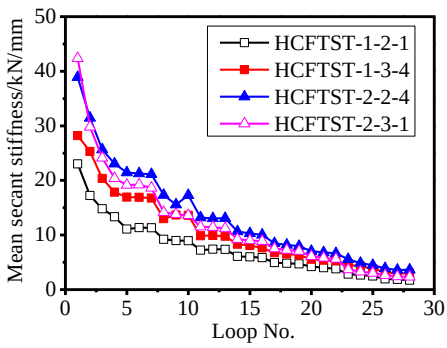

(b) Stiffness degradation of group II

Fig. 10 Analysis of stiffness degradation

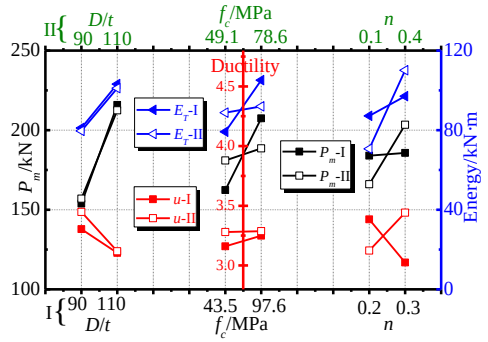

Fig. 11 Influences of the tested parameters

likewise, the relevant indices in group II, respectively, had an increase of 55.94% and 22.55%. In addition, the ductility coefficient in group I decreased by 10.68%, on the contrary the ductility coefficient in group II increased by 10.14%. It was because the concrete strength disparity in group I was larger than that in group II, in this case the improved confining effect induced by increasing axial compression ratio scarcely ameliorated the non-negligible brittleness of HS concrete (f_c = 97.6 MPa), thus the gradual reduction in the effective compression zone of core concrete resulted in a weak deformation capacity. It is noted that a reasonable performance-based design method for Q690 circular HCFTST columns should perform an optimized combination based on the performance indices of energy dissipation, load-resisting capacity and ductility.

4. Shear capacity of HCFTST columns

Similarly to the shear strength of reinforced concrete members, the shear-resisting capacity of a Q690 circular HCFTST column can be the superposition of the steel tube shear-resisting mechanism (V_s), core concrete shear-resisting mechanism (V_c) and contribution attributed to the axial load (V_p) (Priestley *et al*. 1994, Zhou and Liu 2010, Chen *et al*. 2011). Therefore, the nominal shear capacity (V_A) can be derived by

$$V_A = V_s + V_c + V_p \tag{5}$$

where V_s can be the sum of the direct shear-resisting capacity (V_τ) and the shear strength of truss mechanism ($V_{\sigma h}$). As a result, the steel tube can resist the shear force through the tensile strength of a truss model and the direct shear strength by considering the tube acting as a series of independent longitudinal and transverse reinforcing bars (Zhou and Liu 2010).

The direct shear-resisting capacity (V_τ) of a steel tube is illustrated in Fig. 12(a). The maximum shear stress can be calculated by

$$\tau_{\max} = \frac{V_\tau S_z^*}{I_z(2\delta)} = \frac{V_\tau \times 2r_0^2\delta}{\pi r_0^3\delta \times 2\delta} = 2\frac{V_\tau}{A_s} \tag{6}$$

where I_z and S_z^* are the moment of inertia and area moment of the steel tube around *z*-axis, respectively; A_s is the area of steel tube, namely $A_s = 2\pi r_0\delta$. In a circular steel tube, the maximum hoop stress can be taken as $0.19f_y$ (Sakino *et al*. 2004), consequently, the direct shear-resisting capacity (V_τ) can be determined as $V_\tau = 0.5A_s\tau_{\max} = 0.5A_s \times (0.19f_y)$.

With regard to the shear strength of truss mechanism ($V_{\sigma h}$), it is assumed that in the compression zone of the column, however, any cracks are closed by definition, therefore, the shear force cannot be transferred across it by tension strain in the transverse reinforcement (Kowalsky and Priestley 2000). According to Fig. 12(b), a revised truss component equation can be obtained by Eq. (7)

$$V_{\sigma h} = 0.5\pi\delta f_{\sigma h}(D-c)\cot\theta \tag{7}$$

where c is the neutral axis depth (Zhong 2003); the transverse stress $f_{\sigma h}$ is approximately equal to $0.19f_y$ (Sakino *et al*. 2004); θ is the assumed inclination angle between a shear crack and the vertical column axis, which is determined based on the principle of minimum energy (Kim and Mander 2007)

$$\theta = \tan^{-1}\left(\frac{\left(\frac{\rho_v}{\rho_t}\right)\left(\frac{A_v}{A_g}\right)}{1.22}\right)^{\frac{1}{4}} \tag{8}$$

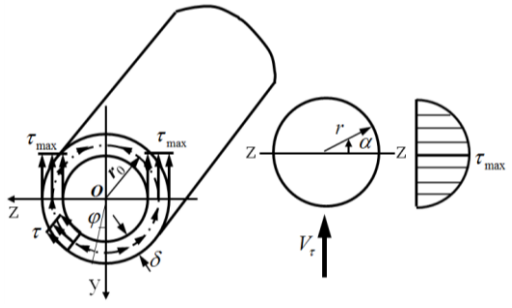

(a) Direct shear-resisting capacity

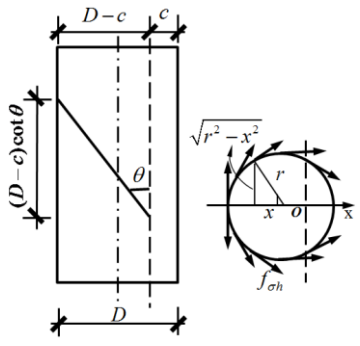

(b) Shear strength of truss mechanism

Fig. 12 Shear-resisting mechanism of the steel tube

where $\rho_v = 2\delta/D$ is the volumetric ratio of shear steel to concrete; $\rho_t = A_s/A_g$ is the ratio of steel tube area to gross cross-sectional area (A_g); A_v is the shear area of core concrete.

The core concrete shear-resisting mechanism (V_c) (Kowalsky and Priestley 2000) can be expressed as

$$V_c = 0.29\sqrt{f_c}\left(0.8A_c\right) \tag{9}$$

Additionally, the contribution attributed to the axial load (V_p) (GB 50936-2014) can be derived by

$$V_p = 0.1P\left(1-0.45\sqrt{\frac{a}{D}}\right) \tag{10}$$

where P is the applied axial compression load, and a is the shear span. Consequently, the nominal shear capacity (V_A) of a Q690 circular HCFTST column can be determined through

$$V_A = V_t + V_{\sigma h} + V_c + V_p \tag{11}$$

Afterwards, the accuracy of the proposed simplified shear strength model was evaluated by comparing the results of the test and the design equation codified in GB 50936-2014, as shown in Table 4, where the shear bearing capacity (P_{mT}) of the tested HCFTST columns was equal to the peak lateral load (P_m) in Table 3 through the mechanical equilibrium principle, because the lateral load of quasi-static test actually produced lateral shear effect to short HCFTST columns. The comparison results indicated that a comparatively good agreement (P_{mP}/P_{mT}) of the simplified model was achieved with a mean value and variance, respectively, of 1.12 and 0.00487 compared to the corresponding values of 1.46 and 0.00485 of the prediction results (P_{mG}/P_{mT}) in GB 50936-2014. The simplified shear strength model in this study is deemed useful for estimating the basic design quality of Q690 circular HCFTST column. However, the proposed model naturally ignored the influences of the bond-slip behavior between the HS thin-walled steel tube and core concrete, the Bauschinger effect and kinematic hardening of the HS steel, and deterioration effects induced by low-cycle fatigue. Development of a more accurate shear strength model is a subject of continuing study.

5. Numerical modeling

Fracture is an important mode of failure in steel structures, especially for the HS steel, therefore an accurate assessment of fracture is significant for developing fracture-resistant design provisions and for evaluating structural performance under extreme loads (e.g., earthquake) (Kanvinde and Deierlein 2006). The test results in this study and literature (Skalomenos *et al*. 2016) proved that CFST columns using HS steel tended to behave a ductile fracture and severe local buckling, indicating an effective fracture damage simulation method to predict the mentioned failure pattern is urgently needed. This section mainly aimed at providing a finite element analysis (FEA) model established in ABAQUS, focusing on the simulation of the fracture behavior of HS steel. The basic information for the FEA model is as follows.

5.1 Constitutive model of steel including fracture

A bilinear kinematic hardening model (Fig. 13) was adopted to simulate the hysteretic behavior of HS steel before the damage initiation (Jiang and Lu 2005).

As the yield stress evolves into post-peak stage, fracture or damage is assumed to initiate (as show in Fig. 14) when the equivalent plastic strain ($\bar{\varepsilon}^{pl}$) reaches the fracture initiation strain ($\bar{\varepsilon}_0^{pl}$) that mainly depends on the stress triaxiality (η), namely

$$\bar{\varepsilon}^{pl} = \bar{\varepsilon}_0^{pl}(\eta) \tag{12}$$

where η is defined as the ratio of the hydrostatic mean stress (σ_m) to the Von Mises equivalent stress ($\bar{\sigma}$)

$$\eta = \frac{\sigma_m}{\bar{\sigma}} = \frac{(\sigma_1+\sigma_2+\sigma_3)/3}{\sqrt{\frac{1}{2}\left[(\sigma_1-\sigma_2)^2+(\sigma_2-\sigma_3)^2+(\sigma_3-\sigma_1)^2\right]}} \tag{13}$$

where σ_1, σ_2 and σ_3 denote principle stresses. Therefore, a fracture initiation criterion (Yu and Jeong 2010) for HS steel is herein expressed as

Table 4 Comparisons between the predicted results and test results

Specimen	f_c/MPa	f_y/MPa	P_{mT}/kN	P_{mP}/kN	P_{mP}/P_{mT}	P_{mG}/kN	P_{mG}/P_{mT}
HCFTST-1-1-2	43.5	723	130.49	163.33	1.25	168.27	1.29
HCFTST-1-4-3	97.6	723	177.25	191.66	1.08	239.72	1.35
HCFTST-2-1-3	43.5	723	194.19	223.74	1.15	297.38	1.53
HCFTST-2-4-2	97.6	723	237.53	247.66	1.04	421.00	1.77
HCFTST-1-2-1	49.1	723	134.45	159.60	1.19	171.26	1.27
HCFTST-1-3-4	78.6	723	179.48	191.65	1.07	220.94	1.23
HCFTST-2-2-4	49.1	723	227.37	237.52	1.04	318.23	1.40
HCFTST-2-3-1	78.6	723	197.55	224.30	1.14	365.90	1.85

* P_{mT}, P_{mP} and P_{mG} denote the shear-resisting capacity derived from the test, the simplified shear strength model and the calculation result by GB 50936-2014, respectively.

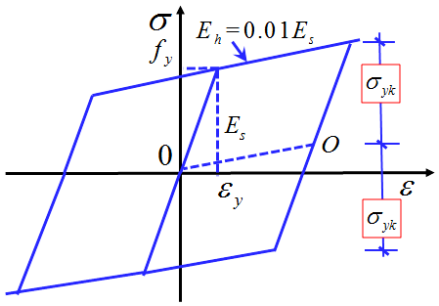

Fig. 13 Constitutive model before damage initiation

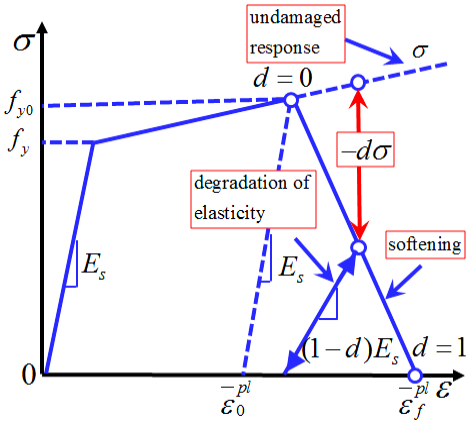

Fig. 14 Damage initiation and evolution of HS steel

$$\bar{\varepsilon}_0^{pl} = \begin{cases} \infty & \eta \le -1/3 \\ C_1/(1+3\eta) & -1/3 < \eta \le 0 \\ C_1 + (C_2 - C_1)(\eta/\eta_0)^2 & 0 \le \eta \le \eta_0 \\ C_2\eta_0/\eta & \eta_0 \le \eta \end{cases} \quad (14)$$

where C_1 is $\bar{\varepsilon}_0^{pl}$ in $\eta = 0$ and C_2 is $\bar{\varepsilon}_0^{pl}$ in $\eta = \eta_0 = 1/3$. In this study, the relevant values of HS steel were adopted as $C_1 = 0.3$ and $C_2 = 0.743$ (Yu and Jeong 2010, Zhou *et al*. 2014, Liao *et al*. 2016); and considering the slight effect on fracture in a quasi-static test, the strain rate adopted a value of 0.001/s in the analysis procedure of ABAQUS (Javidan *et al*. 2016). Consequently, the damage is initiated upon satisfying the following condition

$$\omega_D = \int \frac{d\bar{\varepsilon}^{pl}}{\bar{\varepsilon}_0^{pl}} = 1 \quad (15)$$

where ω_D is a state variable that increases monotonically with plastic deformation.

With the onset of damage, the yield stress softens and the elastic modulus degrades until the equivalent plastic strain reaches failure strain ($\bar{\varepsilon}_f^{pl}$). To enhance the computational efficiency and reduce the mesh dependency, a linear damage evolution law was adopted based on the average equivalent plastic deformation (u_f^{pl} = 4.2 mm) determined by the material test.

5.2 Constitutive model of core concrete

Previous researches indicate the confining effect of steel tube can enhance the strength and ductility of the confined concrete, reflecting that the enhancements of strength and ductility of concrete can be achieved by adopting an equivalent uniaxial stress-strain relationship (Han and Yang 2005, Han *et al*. 2006). Therefore, a uniaxial constitutive model in compression proposed by Sakino *et al*. (2004) was utilized in this FEA model and can be expressed as follows

$$Y = \frac{VX + (W-1)X^2}{1 + (V-2)X + WX^2} \quad (16)$$

$$V = E_c\varepsilon_{cc0} / f_{ccb} \quad (17)$$

$$W = 1.50 - 17.1\times10^{-3} f_c + 2.39\sqrt{f_{re}} \quad (18)$$

where X and Y represent the concrete stress (σ_c) and strain (ε_c), respectively, normalized by the corresponding peak stress (f_{ccb}) and peak strain (ε_{cc0}); V and W are parameters that express the stress-strain relationship for concrete; the parameters f_c and f_{re} are the compressive cylinder strength and the effective lateral pressure, respectively; and E_c is the Young's modulus of the concrete. Besides, the uniaxial tensile stress-strain relationship specified in GB 50010-2010 was introduced in the FEA model. Furthermore, the concrete damage plasticity (CDP) model provided in ABAQUS was utilized to depict the cyclic behavior of core concrete, and the plasticity parameters and damage variables for CDP model were recommended in previous studies (Lee and Fenves 1998, Li *et al*. 2017). Therefore, the hysteretic constitutive model for concrete in this study was formed in Fig. 15, in which the elastic modulus degrades gradually compared to the initial tangent modulus (E_0). The factors w_t and w_c control the recovery of the tensile and compressive stiffness under the reversed loading, and the default setting (w_t = 0, w_c = 1) of recovery factors was adopted in this FEA model.

5.3 Elements and boundary conditions

In this FEA model, the core concrete was modeled using 8-node three-dimensional solid elements. The steel tubes were modeled using 4-node shell elements with full integration. The Coulomb friction model and hard contact were applied in the tangential direction and the normal direction, respectively, for the interaction between the concrete and steel tube (Ma *et al*. 2017). A fixed boundary condition was utilized at the column base, and an axial load combined with a lateral cyclic load was imposed on the top of the column. Subsequently, a mesh convergence study was performed to identify an appropriate mesh density to achieve reliable results with reasonable computation times.

5.4 Results and discussion

To validate the accuracy of the FEA model, the numerical results were compared with the experimental results in terms of the damage mode and load-displacement

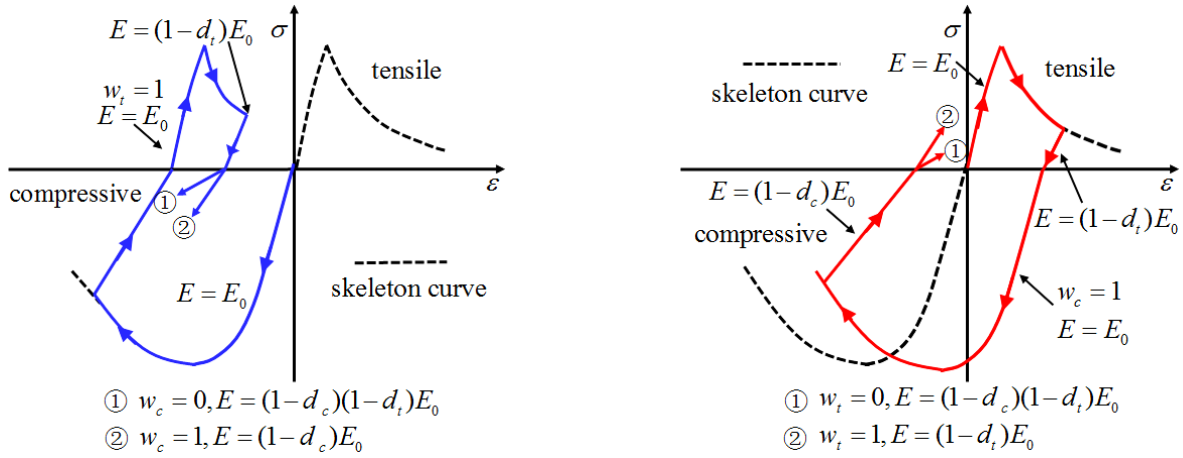

(a) Hysteretic behavior from tension to compression (b) Hysteretic behavior from compression to tension

Fig. 15 Hysteretic constitutive model of concrete

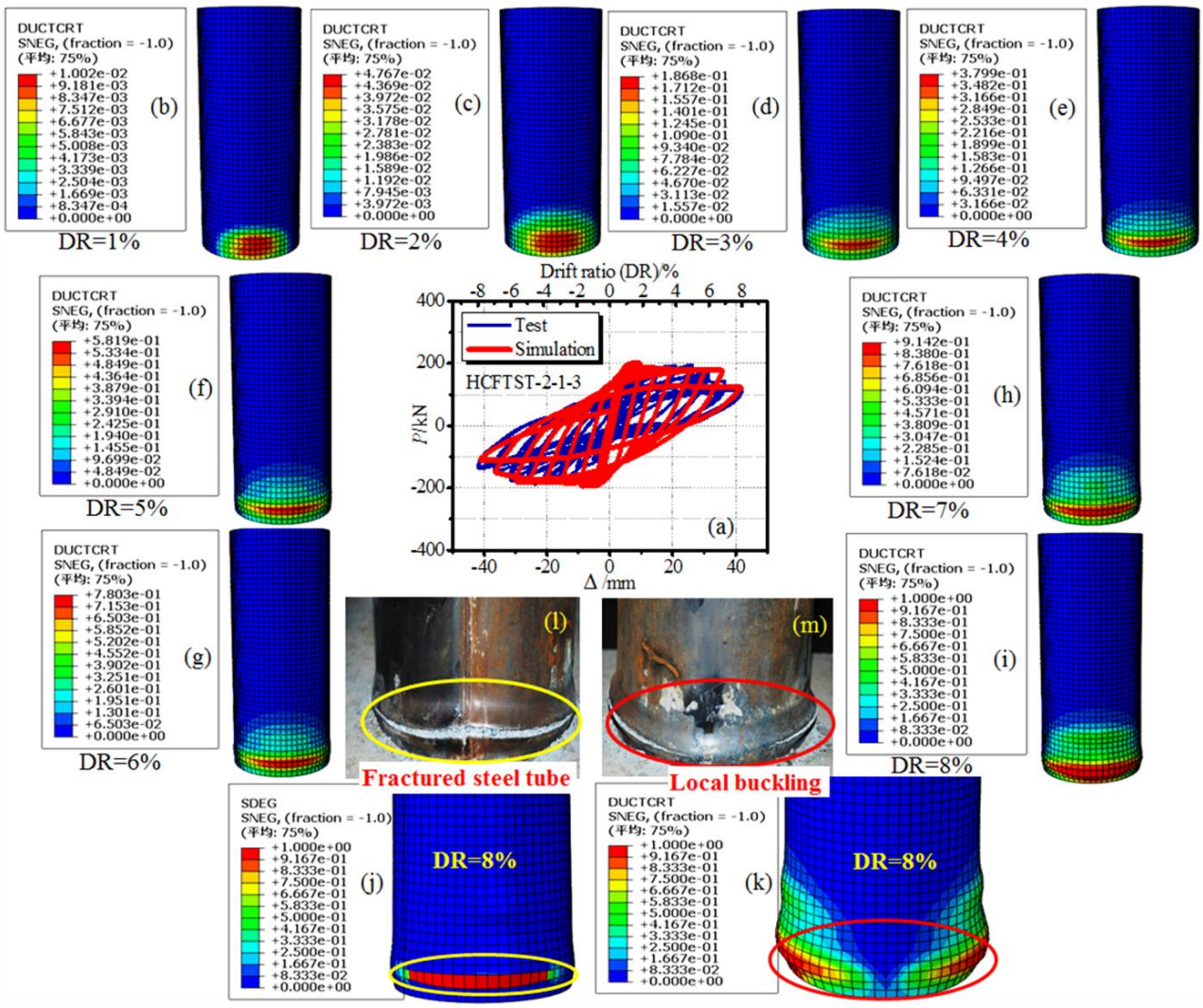

Fig. 16 Comparison of experimental and numerical results

hysteretic curves. Due to the page limit, a typical example of comparison (HCFTST-2-1-3) is shown in Fig. 16 to illustrate the damage process. Fig. 16(a) demonstrates the comparison of load-displacement hysteretic curves, indicating that the simulated hysteresis loops agreed reasonably well with the experimental results in the

degradations of load-resisting capacity and stiffness. Figs. 16(b)~(i) illustrate the accumulation procedure of equivalent plastic deformation, in which a plastic hinge in the column foot gradually developed in combination with an equivalent plasticity ratio ranging from 0.91 to 1.00 at 7%~8% drift, thereby reflecting the steel tube would fracture. Additionally, the simulated failure modes of fracture and local buckling were compared with the test results in Figs. 16(j)~(m). It can be observed the proposed FEA model could accurately simulate the steel fracture and elephant foot shaped local buckling of Q690 circular HCFTST column under cyclic loading. It should be noted that the failure mode at the column foot of HCFTST column was induced by the ultimate bearing capacity state in coupling effect of the bending moment and shear force. Nevertheless, certain differences were observed among the comparison results. The numerical unloading and reloading stiffness of the hysteretic curves differed from the test result, which was likely ascribed to the uncertainties in the actual concrete strength and elastic modulus. In general, the FEA model including fracture damage can accurately predict the damage behavior of Q690 circular HCFTST column under cyclic loading.

6. Conclusions

This paper presents a systematic study on the seismic behavior of Q690 HCFTST columns. Some significant conclusions can be drawn within the scope of this research:

- The Q690 circular HCFTST columns (e.g., HCFTST-1-1-2 and HCFTST-1-2-1) with the NS concrete (f_c = 43.5 MPa, 49.1 MPa) and lower axial compression ratios ($n \leq 0.2$) performed slim hysteretic loops, reflecting that the HS thin-walled steel tube matched with the NS core concrete could hardly motivate enough composite action for enhancing seismic behavior under the lower axial compression ratio. The columns with NS concrete and larger axial compression ratios (e.g., HCFTST-2-1-3 and HCFTST-2-2-4) increased by 13.56% and 7.70% in the normalized energy dissipation, respectively, than those columns with the HS concrete and lower axial compression ratios (e.g., HCFTST-2-4-2 and HCFTST-2-3-1), highlighting that a favorable energy dissipation capacity can be obtained by moderately increasing the axial compression ratio rather than only increasing concrete strength.
- A relatively reasonable ductility deformation capacity could be guaranteed though the ductility coefficient was smaller than that of traditional CFST columns. The effects of the tested parameters on seismic behavior were discussed in detail, e.g., compared to the D/t ratio and axial compression ratio, improving the concrete compressive strength (e.g., the HS thin-walled steel tube filled with HS concrete) had a slight influence on the ductility but an obvious enhancement of energy dissipation and peak load.
- A simplified shear strength model for the Q690 circular HCFTST column was derived by the superposition of the direct shear-resisting capacity (V_τ) and shear strength of truss mechanism ($V_{\sigma h}$) for a steel tube, core concrete shear-resisting mechanism (V_c) and contribution attributed to the axial load (V_p). The proposed shear strength model is deemed useful for estimating the basic design quality of Q690 circular HCFTST column.
- Finally, a finite element analysis (FEA) model incorporating a stress triaxiality dependent fracture criterion was developed and validated to simulate the seismic behavior (e.g., hysteretic curve, local buckling and fracture). The modeling method can be applied to the seismic analysis and design of Q690 circular HCFTST columns.

Acknowledgments

This research work was financially supported by the National Natural Science Foundation of China (Grant No. 11172226; No. 51758094), Scientific Research Project of Shaanxi Provincial Department of Education (No. 18JK1105) and the Fundamental Research Funds for the Central Universities (xzy022019048); their support is gratefully acknowledged. The authors are also grateful to everyone participating in this experimental program for their selfless assistance.

References

ANSI/AISC 360-16 (2016), Specification for structural steel buildings, American National Standards Institute; Chicago, IL, USA.

Boyd, P.F., Cofer, W.F. and Mclean, D.I. (1995), "Seismic performance of steel-encased concrete columns under flexural loading", *ACI Struct. J.*, **92**(3), 355-364.

Chen, S.J., Yang, K.C., Lin, K.M. and Wang, C.D. (2011), "Seismic behavior of ductile rectangular composite bridge piers", *Earthq. Eng. Struct. Dyn.*, **40**(1), 21-34. https://doi.org/10.1002/eqe.1018

Cheng, C.S. (1995), "Some projection properties of orthogonal arrays", *Ann. Stat.*, **23**(4), 1223-1233.

Elremaily, A. and Azizinamini, A. (2002), "Behavior and strength of circular concrete-filled tube columns", *J. Constr. Steel Res.*, **58**(12), 1567-1591. https://doi.org/10.1016/S0143-974X(02)00005-6

Fam, A., Qie, F.S. and Rizkalla, S. (2004), "Concrete-filled steel tubes subjected to axial compression and lateral cyclic loads", *J. Struct. Eng.*, **130**(4), 631-640. https://doi.org/10.1061/(ASCE)0733-9445(2004)130:4(631)

GB 50010-2010 (2010), Code for design of concrete structures, Professional Standard of the People's Republic of China; Beijing, China.

GB 50936-2014 (2014), Technical code for concrete filled steel tubular structures, Professional Standard of the People's Republic of China; Beijing, China.

Gupta, V.K., Nigam, A.K. and Dey, A. (1982), "Orthogonal main-effect plans for asymmetrical factorials", *Technometrics*, **24**(2), 135-137.

Hajjar, J.F., Gourley, B.C. and Olson, M.C. (1997), "A cyclic nonlinear model for concrete-filled tubes. II: verification", *J.*

Struct. Eng., **123**(6), 745-754. https://doi.org/10.1061/(ASCE)0733-9445(1997)123:6(745)

Han, L.H. and Yang, Y.F. (2005), "Cyclic performance of concrete-filled steel CHS columns under flexural loading", *J. Constr. Steel Res.*, **61**(4), 423-452. https://doi.org/10.1016/j.jcsr.2004.10.004

Han, L.H., Huang, H., Tao, Z. and Zhao, X.L. (2006), "Concrete-filled double skin steel tubular (CFDST) beam–columns subjected to cyclic bending", *Eng. Struct.*, **28**(12), 1698-1714. https://doi.org/10.1016/j.engstruct.2006.03.004

Han, L.H., Li, W. and Bjorhovde, R. (2014), "Developments and advanced applications of concrete-filled steel tubular (CFST) structures: Members", *J. Constr. Steel Res.*, **100**, 211-228. https://doi.org/10.1016/j.jcsr.2014.04.016

Hedayat, A.S., Sloane, N.J.A. and Stufken, J. (2012), *Orthogonal Arrays: Theory and Applications*, Springer Science & Business Media, Berlin, Germany.

Huang, Z., Jiang, L.Z., Chen, Y.F., Luo, Y. and Zhou, W.B. (2018), "Experimental study on the seismic performance of concrete filled steel tubular laced columns", *Steel Compos. Struct., Int. J.*, **26**(6), 719-731. https://doi.org/10.12989/scs.2018.26.6.719

Inai, E., Mukai, A., Kai, M., Tokinoya, H., Fukumoto, T. and Mori, K. (2004), "Behavior of concrete-filled steel tube beam columns", *J. Struct. Eng.*, **130**(2), 189-202. https://doi.org/10.1061/(ASCE)0733-9445(2004)130:2(189)

Javidan, F., Heidarpour, A., Zhao, X.L. and Minkkinen, J. (2016), "Application of high strength and ultra-high strength steel tubes in long hybrid compressive members: Experimental and numerical investigation", *Thin-Wall. Struct.*, **102**, 273-285. https://doi.org/10.1016/j.tws.2016.02.002

Javidan, F., Heidarpour, A., Zhao, X.L. and Al-Mahaidi, R. (2018), "Structural coupling mechanism of high strength steel and mild steel under multiaxial cyclic loading", *Steel Compos. Struct., Int. J.*, **27**(2), 229-242. https://doi.org/10.12989/scs.2018.27.2.229

Jiang, J.J. and Lu, X.Z. (2005), *Finite Element Analysis of Concrete Structures*, Tsinghua University Press, Beijing, China.

Kanvinde, A.M. and Deierlein, G.G. (2006), "The void growth model and the stress modified critical strain model to predict ductile fracture in structural steels", *J. Struct. Eng.*, **132**(12), 1907-1918. https://doi.org/10.1061/(ASCE)0733-9445(2006)132:12(1907)

Kim, J.H. and Mander, J.B. (2007), "Influence of transverse reinforcement on elastic shear stiffness of cracked concrete elements", *Eng. Struct.*, **29**(8), 1798-1807. https://doi.org/10.1016/j.engstruct.2006.10.001

Kowalsky, M.J. and Priestley, M.N. (2000), "Improved analytical model for shear strength of circular reinforced concrete columns in seismic regions", *ACI Struct. J.*, **97**(3), 388-396.

Lee, J. and Fenves, G.L. (1998), "Plastic-damage model for cyclic loading of concrete structures", *J. Eng. Mech.*, **124**(8), 892-900. https://doi.org/10.1061/(ASCE)0733-9399(1998)124:8(892)

Li, T.J., Li, G.Q., Chan, S.L. and Wang, Y.B. (2016), "Behavior of Q690 high-strength steel columns: Part 1: Experimental investigation", *J. Constr. Steel Res.*, **123**, 18-30. https://doi.org/10.1016/j.jcsr.2016.03.026

Li, C., Hao, H. and Bi, K. (2017), "Numerical study on the seismic performance of precast segmental concrete columns under cyclic loading", *Eng. Struct.* **148**, 373-386. https://doi.org/10.1016/j.engstruct.2017.06.062

Liao, F.F., Li, W.C. and Zhou, T.H. (2016), "Experimental study on fracture characteristics of Q460D high strength steel and calibration of fracture criterion", *J. Xi'an Univ. Arch. Tech. (Natural Science Edition)*, **48**(3), 362-370.

Ma, D.Y., Han, L.H., Li, W. and Zhao, X.L. (2017), "Seismic Performance of concrete-encased CFST piers: analysis", *J. Bridge. Eng.*, **23**(1), 04017119. https://doi.org/10.1061/(ASCE)BE.1943-5592.0001157

Marson, J. and Bruneau, M. (2004), "Cyclic testing of concrete-filled circular steel bridge piers having encased fixed-based detail", *J. Bridge Eng.*, **9**(1), 14-23. https://doi.org/10.1061/(ASCE)1084-0702(2004)9:1(14)

Nakanishi, K., Kitada, T. and Nakai, H. (1999), "Experimental study on ultimate strength and ductility of concrete filled steel columns under strong earthquake", *J. Constr. Steel Res.*, **51**(3), 297-319. https://doi.org/10.1016/S0143-974X(99)00006-1

Portoles, J.M., Serra, E. and Romero, M.L. (2013), "Influence of ultra-high strength infill in slender concrete-filled steel tubular columns", *J. Constr. Steel Res.*, **86**, 107-114. https://doi.org/10.1016/j.jcsr.2013.03.016

Priestley, M.N., Seible, F., Xiao, Y. and Verma, R. (1994), "Steel jacket retrofitting of reinforced concrete bridge columns for enhanced shear strength-part 1: Theoretical considerations and test design", *ACI Struct. J.*, **91**(4), 394-405.

Sakino, K. (1981), "Hysteretic behavior of concrete filled squara steel tubular beam-columns failed in flexure", *Trans. Jpn. Concr. Inst.*, **3**, 439-446.

Sakino, K., Nakahara, H., Morino, S. and Nishiyama, I. (2004), "Behavior of centrally loaded concrete-filled steel-tube short columns", *J. Struct. Eng.*, **130**(2), 180-188. https://doi.org/10.1061/(ASCE)0733-9445(2004)130:2(180)

Skalomenos, K.A., Hayashi, K., Nishi, R., Inamasu, H. and Nakashima, M. (2016), "Experimental behavior of concrete-filled steel tube columns using ultrahigh-strength steel", *J. Struct. Eng.*, **142**(9), 04016057. https://doi.org/10.1061/(ASCE)ST.1943-541X.0001513

Usami, T. and Ge, H. (1994), "Ductility of concrete-filled steel box columns under cyclic loading", *J. Struct. Eng.*, **120**(7), 2021-2040. https://doi.org/10.1061/(ASCE)0733-9445(1994)120:7(2021)

Varma, A.H., Ricles, J.M., Sause, R. and Lu, L.W. (2002), "Seismic behavior and modeling of high-strength composite concrete-filled steel tube (CFT) beam–columns", *J. Constr. Steel Res.*, **58**(5-8), 725-758. https://doi.org/10.1016/S0143-974X(01)00099-2

Varma, A.H., Ricles, J.M., Sause, R. and Lu, L.W. (2004), "Seismic behavior and design of high-strength square concrete-filled steel tube beam columns", *J. Struct. Eng.*, **130**(2), 169-179. https://doi.org/10.1061/(ASCE)0733-9445(2004)130:2(169)

Wu, C.J. and Hamada, M.S. (2011), *Experiments: Planning, Analysis, and Optimization*, John Wiley & Sons, Hoboken, USA.

Xue, J., Zhou, C. and Lin, J. (2018), "Seismic performance of mixed column composed of square CFST column and circular RC column in Chinese archaized buildings", *Steel Compos. Struct., Int. J.*, **29**(4), 451-464. https://doi.org/10.12989/scs.2018.29.4.451

Yu, H.L. and Jeong, D.Y. (2010), "Application of a stress triaxiality dependent fracture criterion in the finite element analysis of unnotched Charpy specimens", *Theor. Appl. Fract. Mech.*, **54**(1), 54-62. https://doi.org/10.1016/j.tafmec.2010.06.015

Zhang, G.W., Xiao, Y. and Kunnath, S. (2009), "Low-cycle fatigue damage of circular concrete-filled-tube columns", *ACI Struct. J.*, **106**(2), 151-159.

Zhong, S.T. (2003), *The Concrete-filled Steel Tubular Structures*, Tsinghua University Press, Beijing, China.

Zhou, X. and Liu, J. (2010), "Seismic behavior and shear strength of tubed RC short columns", *J. Constr. Steel Res.*, **66**(3), 385-397. https://doi.org/10.1016/j.jcsr.2009.10.011

Zhou, T., Chen, Z. and Liu, H. (2012), "Seismic behavior of special shaped column composed of concrete filled steel tubes", *J. Constr. Steel Res.*, **75**, 131-141.

https://doi.org/10.1016/j.jcsr.2012.03.015
Zhou, T.H., Li, W.C., Guan, Y. and Bai, L. (2014), "Damage analysis of steel frames under cyclic load based on stress triaxiality", *Eng. Mech.*, **31**(7), 146-155.
Zhu, W., Jia, J., Gao, J. and Zhang, F. (2016), "Experimental study on steel reinforced high-strength concrete columns under cyclic lateral force and constant axial load", *Eng. Struct.*, **125**, 191-204. https://doi.org/10.1016/j.engstruct.2016.07.018
Zhu, W., Jia, J. and Zhang, J. (2017), "Experimental research on seismic behavior of steel reinforced high-strength concrete short columns", *Steel Compos. Struct., Int. J.*, **25**(5), 603-615. https://doi.org/10.12989/scs.2017.25.5.603

DL